Solar Energy Materials and Solar Cells

An international journal devoted to photovoltaic, photothermal and photochemical solar energy conversion

Available online at www.sciencedirect.com

SciVerse ScienceDirect

(This is a sample cover image for this issue. The actual cover is not yet available at this time.)
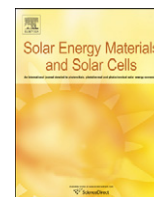
Au–Pt core–shell nanoemitters on silicon for photoelectrochemical solar energy conversion

M. Lublow [a,c,*], B. Bouabadi [b], S. Kubala [c]

[a] Helmholtz-Centre Berlin for Materials and Energy, Institute for Heterogeneous Materials Systems, Berlin, Germany
[b] Ibn Tofail University, Kenitra, Morocco
[c] Fritz-Haber-Institute, Department of Inorganic Chemistry, Department of Physical Chemistry, Berlin, Germany

ARTICLE INFO

ABSTRACT

Electrochemical self-organization principles were applied for nanofabrication of Au–Pt core–shell nanoemitters on pre-structured porous SiO_2/Si interfaces. The silicon templates were fabricated by oscillatory photocurrent cycles in fluoride containing solutions, permitting subsequent local electro-deposition of rectifying metal heterocontacts into the pores. Enhanced light absorption of this Au–Pt/SiO_2/Si nanoarchitecture is deduced from Mie scattering analysis and Finite Difference Time Domain simulations in dependence on the Pt-shell thickness. Test operation as photoelectrochemical cells in I^-/I_3^- redox electrolytes shows conversion efficiencies of 11.6% improving thus the performance of the cells without plasmonic enhancement. It is thereby proven that self-organized electrochemical conditioning on the nanoscale can be successfully applied for preparation of advanced photovoltaic systems, opening thereby new avenues for low-cost production also of solid-state devices.

1. Introduction

Plasmonic nanostructures at the interface of photovoltaic devices are capable to increase the usable amount of photo-induced charge carriers by complemental optical principles [1,2]. Electric field enhancements can significantly raise the generation of electron–hole pairs in a surface-near region and therefore optimize the performance particularly of thin-film solar cells. Increased forward scattering of electromagnetic radiation, on the other hand, can reduce light reflection at the surface and improves therefore the efficiency also of wafer-based systems. Consequently, many novel designs with enhanced light to energy conversion efficiencies were realized in recent investigations and discussed in the literature [3–5]. As in solid-state photovoltaics, also photoelectrochemical systems can considerably benefit from advanced light guiding techniques [6–8]. The exposure of these devices to a redox electrolyte, however, brings about further aspects which can result in beneficial or deleterious effects when metal nanoparticles are present at the solid-liquid interface. Firstly, the plasmonic nanoarchitectures are embedded in a liquid, characterized by specific absorption lines of the redox species in solution and by an index of refraction n > 1. The optical conditions for light absorption and scattering differ therefore from those observed in air or other dielectric environments. Secondly, specific adsorption of ions at the metal surface or metal dissolution in the presence of an external potential can reduce the efficiency of the particles or even destroy them. Surface protection, as of outmost importance for the lifetime of the photoelectrochemical cell, has therefore to be considered individually for the semiconductor interface and the metal clusters.

Here, we describe the preparation and properties of plasmonic Schottky nanocontacts with Au–Pt core–shell-like geometries at a pre-structured SiO_2/Si interface. The cell fabrication is essentially based on electrochemical self-organization phenomena, and first assessment of the cell performance is consequently carried out in the photoelectrochemical mode in an iodide–triiodide (I^-/I_3^-) redox electrolyte. Since Au-nanoparticles (Au-NPs) are susceptible to dissolution in this electrolyte [9], Pt nucleation centers and protective shells were used to prevent the Au nanocores from corrosion. Compared to monometallic Pt nanoemitter interfaces, reported earlier [10,11], this transformation to plasmonic Schottky-junctions has the potential advantage of increased light absorption in a surface-near region over a wide range of the visible spectrum. Fabrication principles are briefly summarized, comprising the preparation of Au–Pt composite structures and the improved protection of the interface region against corrosion in the aqueous electrolyte. Mie theory is applied for comparative assessment of scattering and absorption efficiencies of single monometallic and core–shell spheres. Finite Difference Time Domain (FDTD) simulations are used for the analysis of periodic
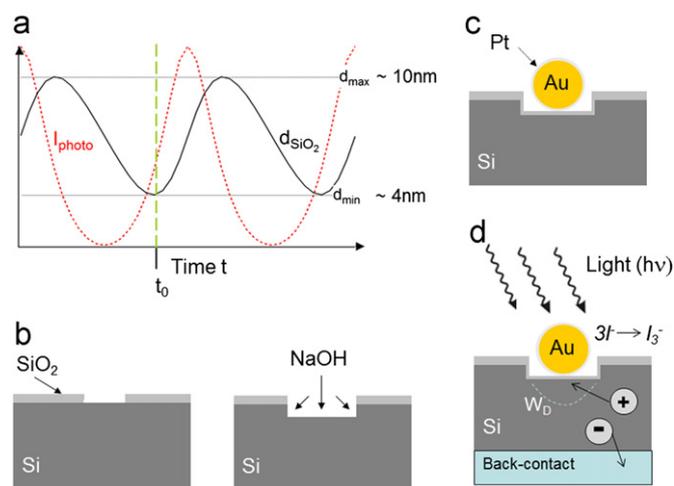
Fig. 1. (Electro)chemical preparation steps of the silicon interface. (a) Schematic of the photocurrent behavior (dotted red curve) and the corresponding SiO_2 thickness variation (solid black curve) during sustained photocurrent oscillations (at pH4). Sample oxidation was stopped at $t=t_0$ (minimum oxide thickness). (b) Cross-sectional view on the porous SiO_2/Si interface (left) and pore deepening by chemical NaOH etching (right). (c) Electrochemical formation of spherical Au–Pt core–shell nanostructures. (d) Operation as photoelectrochemical solar cell in iodide/triiodide. (For interpretation of the references to color in this figure legend, the reader is referred to the web version of this article.)

arrangements of particles at the SiO_2/Si interface. It will be shown that the combination of Au cores and Pt shells results in similar light absorption enhancements as already reported for the Si interface, decorated with monometallic Au-NPs [4,5]. Accordingly, maximum efficiencies for solar light to energy conversion of 11.6% were obtained exceeding those values reported so far for the non-plasmonic device architecture [11,12]. The findings are therefore regarded as important advancement towards future low-cost fabrication of complex solid-state devices by electro-chemical self-organization principles.

2. Experimental

N-type silicon with (100) surface orientation and doping density 10^{15} was used. The samples were etched in a 3:1 mixture of HF(50%) and ethanol for 30 and 10 s with intermediate water rinsing (ultra pure water, 18.2 MΩ) and nitrogen drying. Subsequently, the samples were connected to an electrochemical cell using a Pt counter and a Ag/AgCl reference electrode [13,14]. Photocurrent oscillations were induced at a potential of 6 V in a solution of 0.1 M NH_4F of pH4 and pH2, respectively. The samples were illuminated by a tungsten-iodine lamp (light intensity 80 mW/cm^2). At pH4, sustained photocurrent oscillations can be observed, indicating the repeated oxidation and etching of
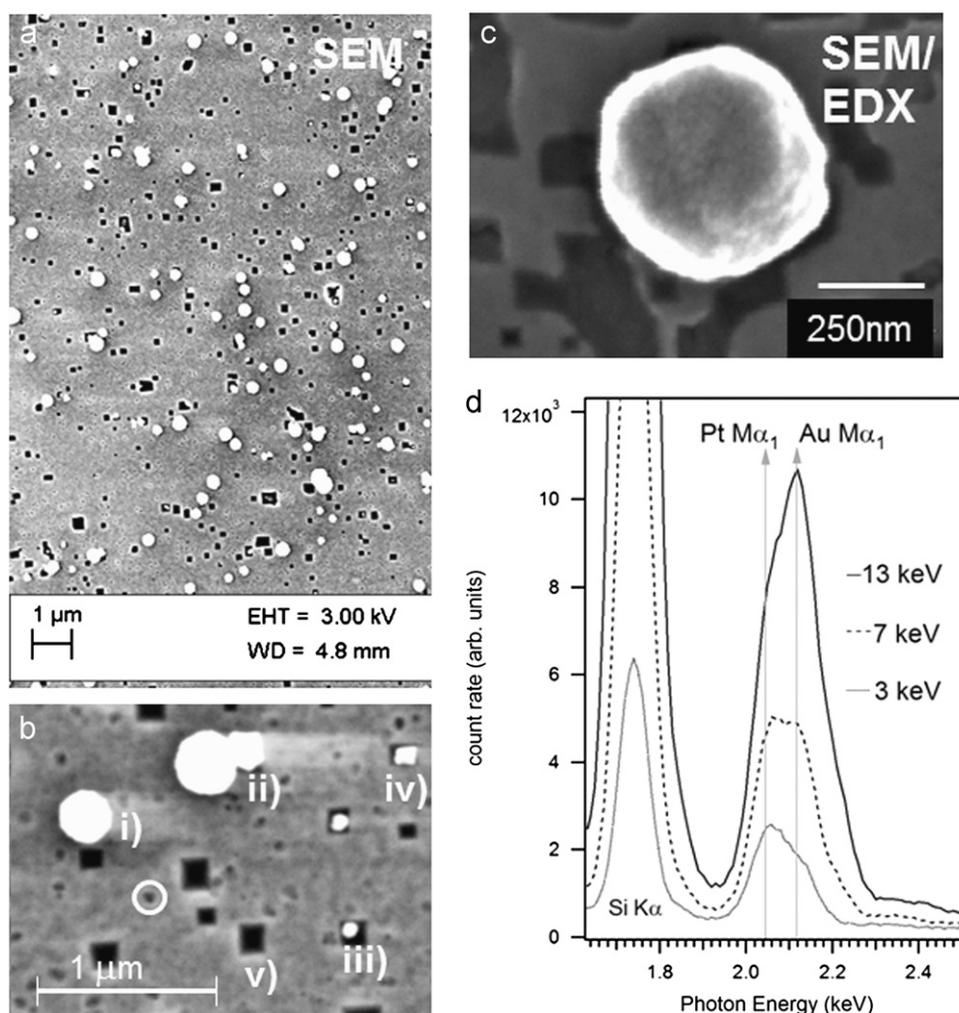
Fig. 2. SEM/EDX analysis of the porous SiO_2/Si interface after formation of spherical Au–Pt core–shell structures. (a) SEM survey of pore and nanoparticle distribution. (b) Magnification with specific particle-pore arrangements (see text). Very small pores are emphasized by a white circle. (c) SEM image of a large metal particle used for EDX analysis. (d) EDX depth analysis of the particle shown in (c). Acceleration energies as well as X-ray detection energies for Pt and Au (and Si) are indicated.

the silicon interface in a self-organized dynamic equilibrium [15]. After a few photocurrent cycles the samples were removed from the cell, at a time t_0 corresponding to about 4 nm thickness of the anodic oxide layer (Fig. 1a). At pH2, the oscillation amplitudes are quickly damped and the photocurrent density (as well as the oxide layer thickness) approaches a steady-state value after about 200 s (compare Fig. 8b). During the oscillatory oxidation of the samples, nanopores are formed in the oxide, partially extending to the silicon interface (Fig. 1b, left). Pore size distribution and density varies for the two pH values as discussed in detail further below. The samples were rinsed and dried and subsequently exposed for 300 s to a solution of 2 M NaOH. During this period of time, anisotropic pore widening and deepening into the Si bulk takes place while the surrounding SiO$_2$ layer is preserved (Fig. 1b, right). Pt and Au were electrodeposited in the potentiostatic mode from 10^{-3} M solutions of H$_2$PtCl$_6$ and HAuCl$_4$, respectively, using 0.1 M KSO$_4$ as supporting electrolyte (Fig. 1c). Charge flow and deposition times were chosen such that small Pt nuclei were formed first ($Q_1 = 1$–2 mC), larger Au structures in the following ($Q_2 = 4$–6 mC) and a finishing Pt layer finally ($Q_3 = 1$–3 mC). The charge flow Q_2 and the ratio of Q_2 and Q_3 served as approximate measure for the Pt shell thickness. Beneath the spherical metal structures, formation of an ultra-thin oxide film is assumed as typically observed upon metal deposition onto silicon, either chemical or electrochemical [11]. The samples were finally tested in an I$^-$/I$_3^-$ redox electrolyte as photoelectrochemical solar cell. Upon illumination (100 mWcm^{-2}), light-induced holes are collected at the metal-oxide-semiconductor space charge region (W_D), initiating the reaction $3I^- + 2h^+ \rightarrow I_3^-$ in solution (Fig. 1d).

The plasmonic activity of the Au–Pt/SiO$_2$/Si interface region was assessed by reflectance measurements of p-polarized light with an angle of incidence close to the Brewster angle of the Si substrate ($\sim 77°$) [16,17]. For analysis of the Si 2p and the Au/Pt 4f core levels, X-ray photoelectron spectroscopy (XPS) was carried out immediately after sample preparation, using a Mg Kα excitation source. Local analysis of the chemical state of the particles and of the surrounding area was performed by Energy Dispersive X-ray analysis (EDX). The surface topography was analyzed by Scanning Electron Microscopy (SEM). Depth analysis of the nanoporous silicon interface was carried out by Tapping-Mode Atomic Force Microscopy (TM-AFM).

3. Results and discussion

3.1. Surface topography and chemistry

Anisotropic etching by 2 M NaOH results in a distribution of rectangular shaped pores in the silicon substrate. Side-walls of the pores are characterized by slow etching (111)-planes as detected by TM-AFM. The pore geometry therefore resembles inverted pyramids. Pore size and, to some extent, pore depth change with exposure time to NaOH while pore density and mutual distances are related to the initial pore distribution in the anodic oxide layer [15]. Diameters of square pores vary between 50 and 200 nm as observed by SEM topographical surface analysis in Fig. 2a and b. For anodic oxides, built in a 0.1 M NH$_4$F solution of pH4, also a large number of very small circular pores (diameter < 20 nm) is visible (see Fig. 2b). The metallic nanostructures, built by consecutive electrodeposition of Pt, Au and Pt, show an average diameter between 100 and 200 nm. Not all pores, however, are filled as shown in Fig. 2a and b. On a magnified scale in Fig. 2b, individual metal-pore arrangements are distinguished: (i) spherical particles completely covering the pore area, (ii) particle coalescence, (iii) small spherical particles fully embedded in the pores, (iv) non-spherical particles and (v) pores not filled by

the metals. Very small pores of circular shape are emphasized by a white circle. EDX depth analysis of the Pt and Au M$_{\alpha 1}$ X-ray emission lines of a single large particle (Fig. 2c) indicates increasing Au-signals with increasing electron acceleration energies (Fig. 2d). The change in the relative contributions of Pt and Au in dependence on the information depth therefore confirms the successful local deposition of the metals atop of each other. For a few particles, particularly of non-spherical shape, no Pt-capping could be detected by local EDX analysis.

XPS results, shown in Fig. 3, prove the simultaneous presence of Au and Pt at the surface as well as of oxidized silicon (not shown here). The photoionization cross section of the Au 4f photoelectron is slightly larger than the corresponding cross section of the Pt 4f electron [18]. The escape depth of Au and Pt photoelectrons is about 3–4 nm only. The relatively large signal of the Au 4f core-level in Fig. 3 points therefore to the presence of particles, not sufficiently covered by Pt, as already deduced from EDX analysis. The cause of imperfect Pt shell formation may be related to electrostatic effects during electrodeposition of the metals. Upon polarization of the interface, electric field lines extend radially from near-spherical metal structures but are distorted at irregularly formed surfaces. These distortions may hamper the formation of a homogeneous Pt-capping layer around non-spherical Au-cores.

3.2. Optical analysis

In the limit of small spherical particles, where the electric field of the incident electromagnetic wave varies little across the particle diameter, cross-sections of absorption and scattering can be expressed by [19,20]

$$C_{sca} = \frac{1}{6\pi}\left(\frac{2\pi}{\lambda}\right)^4 |\alpha|^2 \quad \text{and} \quad C_{abs} = \frac{2\pi}{\lambda}\text{Im}(\alpha). \tag{1}$$
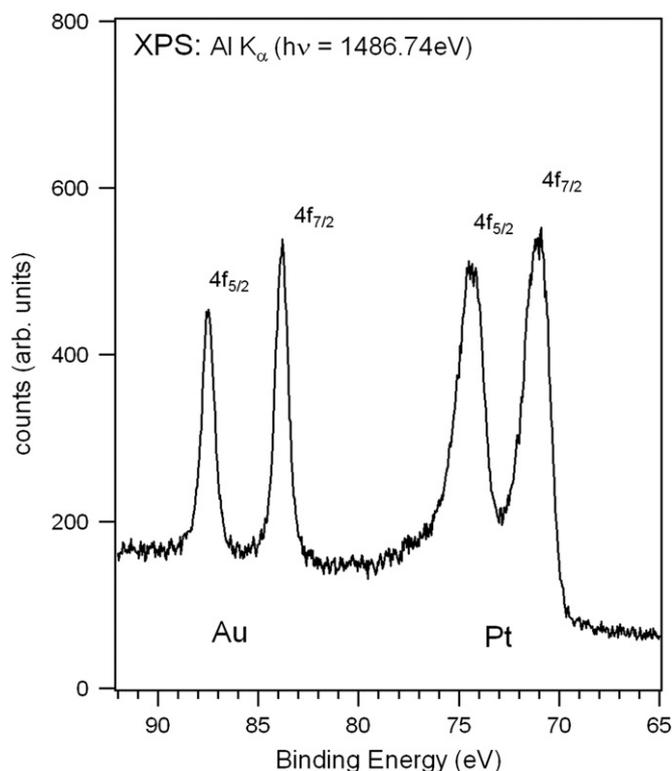
**Fig. 3.** XPS surface analysis of the interface in Fig. 2 employing a monochromatized Al Kα X-ray source. The respective core level signals of Au and Pt 4f electrons are indicated.

Here, λ denotes the wavelength of light and α the (static) polarizability of the metal sphere of radius r, which is given by

$$\alpha = 4\pi\varepsilon_0 r^3 \frac{\varepsilon_m - \varepsilon_a}{\varepsilon_m + 2\varepsilon_a}. \qquad (2)$$

The polarizability depends on the respective permittivity of free space, ε_0, the metal, ε_m, and the ambient, ε_a. From Eq. (1) follows that increased scattering can be expected for larger particle volumes. With increasing particle volume, however, the absorption by the metal increases too, reducing thus the fraction of light which is directed towards the absorbing substrate. Careful design of the plasmonic nanoarchitectures is therefore required in order to ensure efficient light management at the interface.

Although the dipole approximation provides qualitative assessment also for larger particles, Mie theory [21] has to be used for accurate determination of scattering and absorption cross-sections and efficiencies, $C_{sca/abs}$ and $Q_{sca/abs}$, respectively. These quantities are related by: $Q_{sca/abs} = C_{sca/abs}/A$ where A denotes the geometrical cross-section, $A = \pi r^2$. The scattering efficiency, in turn, comprises contributions of forward and backward scattering, i.e. $Q_{sca} = Q_{fwd} + Q_{back}$. In Fig. 4, scattering and absorption efficiencies of Au-, Pt- and Au–Pt core–shell structures were determined, either surrounded by air or by water. Scattering and absorption efficiencies of Platinum spheres show small variations around 600 nm, pointing to low plasmonic activity as recently reported [22]. The corresponding variations of
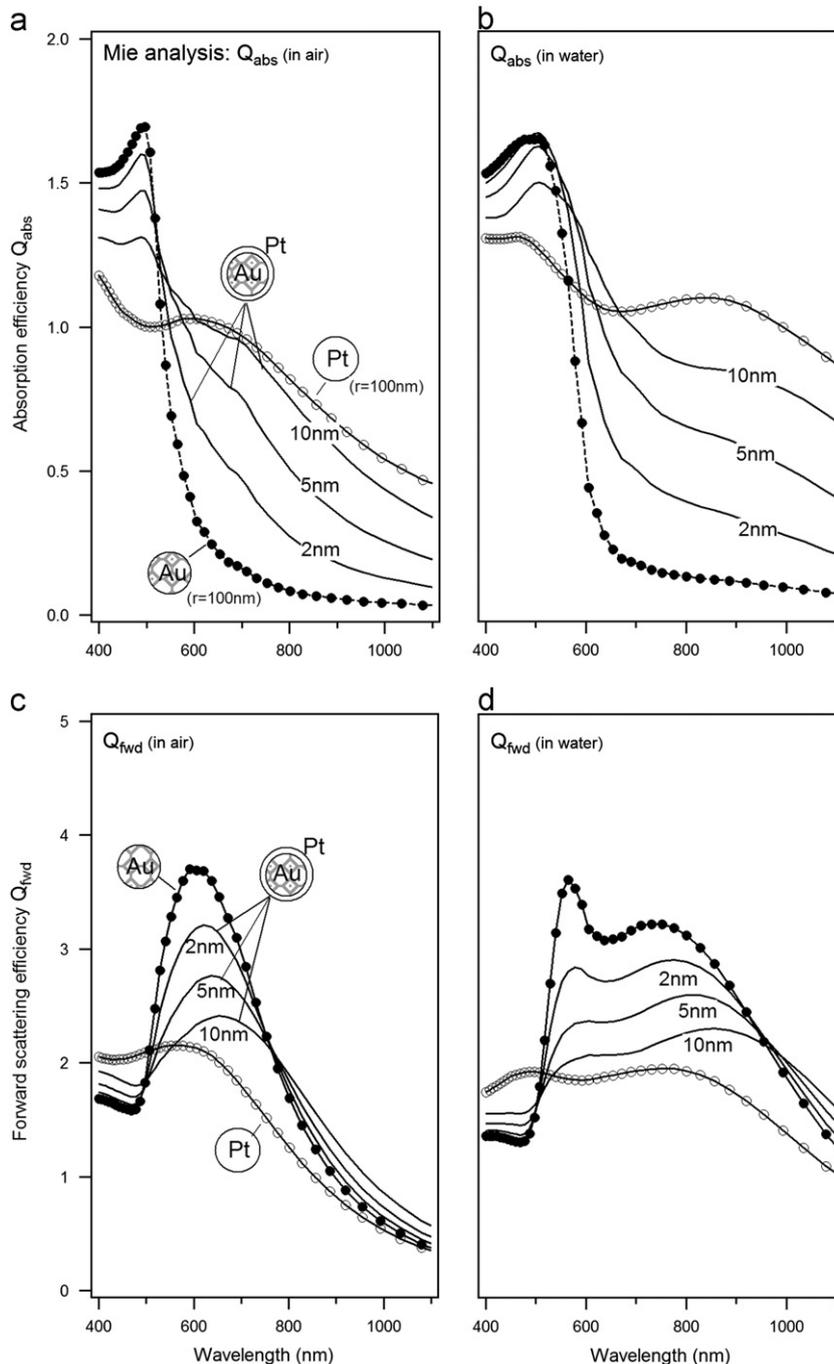

Fig. 4. Mie analysis of spherical Au (solid circles), Pt (open circles) and Au–Pt core–shell nanostructures (solid lines). Absorption efficiencies (in air) are shown in (a). The corresponding values for particles immersed in water are shown in (b). In (c) and (d) the calculated efficiencies for forward scattering are shown.

Au spheres at about 500 nm, in turn, are much more pronounced. For the analysis of Au–Pt core–shell structures, the assumed Pt shell thickness is indicated in Fig. 4 and varies from 2 to 10 nm. Due to the small penetration depth of electromagnetic waves in metals,

$$\delta = \frac{\lambda}{2\pi k}, \tag{3}$$

the absorption behavior of core–shell particles approaches that of Pt upon increasing shell thickness (Fig. 4a and b). In Eq. (3), k denotes the extinction coefficient, i.e. the imaginary component of the generalized index of refraction. Conversely, with decreasing shell thickness, the forward scattering behavior of the core–shell particles approaches that of Au-spheres (Fig. 4c and d). For Pt, the penetration depth of visible light varies between 22 and 25 nm while the corresponding value for Au varies between 32 and 43 nm. Strong field attenuation in the Pt-shells is therefore expected if the Pt-capping exceeds a few nm. In an aqueous environment, compared to air, the efficiencies for absorption and scattering increase, particularly in the near-infrared region of the solar spectrum (compare Fig. 4a and c to b and d, respectively). The dielectric environment can therefore considerably modify the optical interface properties and will be taken into account in a detailed assessment of the actual interface geometry by Finite Difference Time Domain (FDTD) calculations in the following. The geometrical setup is shown in Fig. 5. Electromagnetic fields were calculated in a 500 nm thick silicon slab. Back-reflection at the bottom of the simulation area was excluded by appropriate boundary settings. A periodic arrangement of Au-NPs and Pt-NPs, respectively, was used with particles of radius $r=100$ nm at a mutual distance between 300 and 1000 nm. For simulation of Au–Pt core–shell structures, Pt shells of 2, 5 and 10 nm thickness were assumed. Oxide thicknesses of 10, 4 and 0 nm were taken into account. These layer thicknesses correspond to the maximum and minimum thickness during sustained electrochemical oscillations at pH4 (see Fig. 1a) and to an etched, oxide-free surface, respectively. In order to simplify the interface geometry, the influence of pores in the substrate was ignored. Particles with numbers 3 and 4 in Fig. 5 therefore represent the actual topography, experimentally prepared, while those with numbers 1 and 2 refer to the assumed topography in FDTD calculations.

The absorption enhancement g, i.e. the ratio of the power absorbed by a surface, decorated with particles, and by a bare substrate is shown in Fig. 6a and b. Simulated data for a surface coverage of 20% ($D=400$ nm) and SiO_2 thickness of 4 nm are shown which result in an distinct absorption enhancement in the wavelength range above 600 nm. In the wavelength region below 600 nm, g is smaller than 1 for both dielectric environments, air and water, and for all Au–Pt compositional ratios. In this region, also absorption lines of the I^-/I_3^- redox electrolyte (about 280, 350 and 460 nm) are located with relative intensities depending on solution composition and pH. In the range above 500 nm, an increase of 17% is obtained for the interface exposed to water. In the range between 650 and 1100 nm, the increase amounts even to 30%. Since the optical behavior Au–Pt core–shell structures approaches that of monometallic Au-NPs with decreasing Pt-layer thickness, the corresponding enhancements of 28% and 48%, respectively, represent the possible enhancement limit for the assumed parameters, i.e. particle size and density. Fig. 7 summarizes the potential increase of light absorption in air (Fig. 7a) and in an aqueous environment (Fig. 7b). Here, the differences, Δg, of the respective enhancements obtained by Au–Pt core–shell particles (Pt layer thickness 2 nm) and monometallic Pt structures are shown. It is evident that core–shell structures can result in superior light absorption properties especially in an aqueous
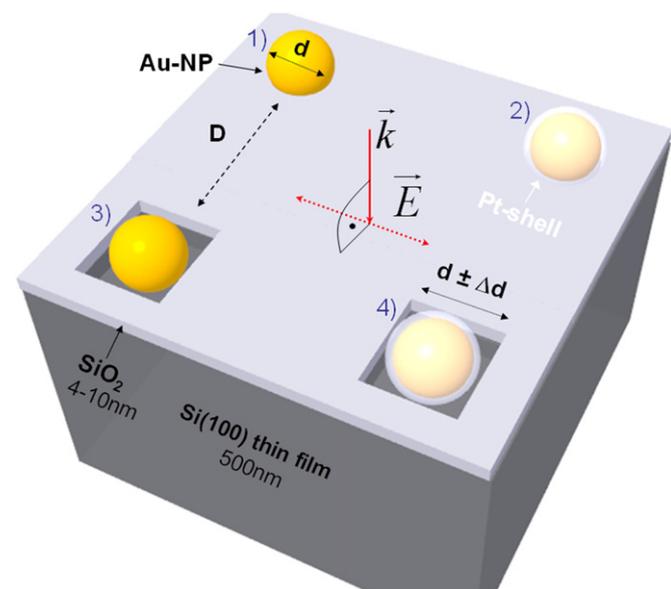

Fig. 5. Setup for FDTD analysis of Au, Pt and Au–Pt core–shell nanospheres at the SiO₂/Si interface. Indicated numbers refer to particle topographies used for the simulation (1 and 2), and those experimentally prepared (3 and 4). Polarized light at normal incidence was assumed. The orientation of the electric field vector is indicated as red dashed arrow.
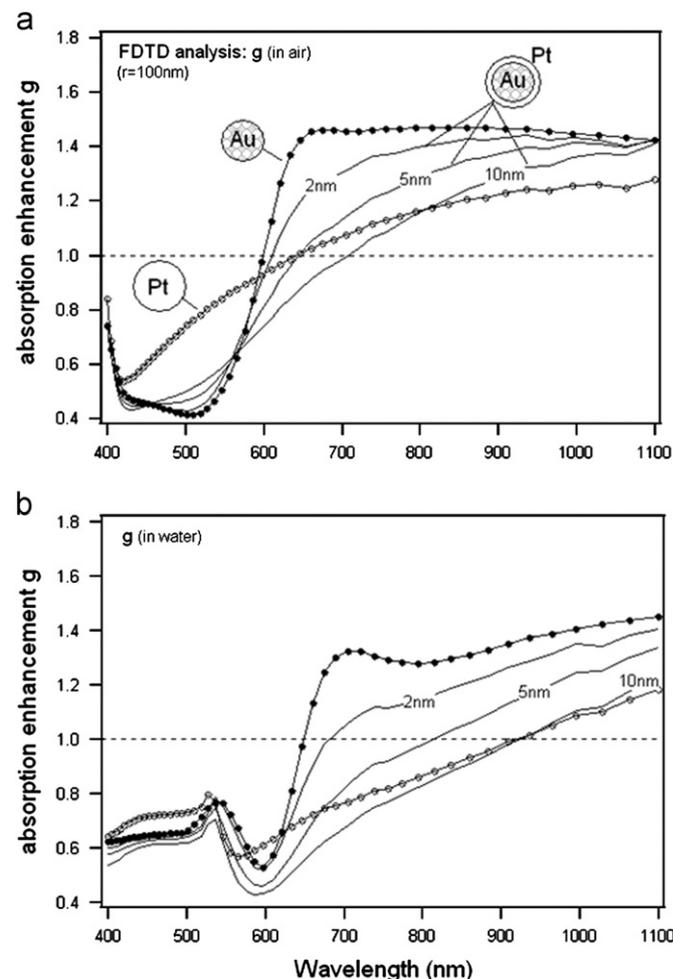

Fig. 6. FDTD calculation of the absorption enhancement of Au (solid circles), Pt (open circles) and Au–Pt core–shell particles (solid curves) embedded in a 4 nm thick SiO₂ mask. (a) Absorption enhancements in air for Pt shell thicknesses of 2, 5 and 10 nm. (b) Corresponding absorption enhancements in water.
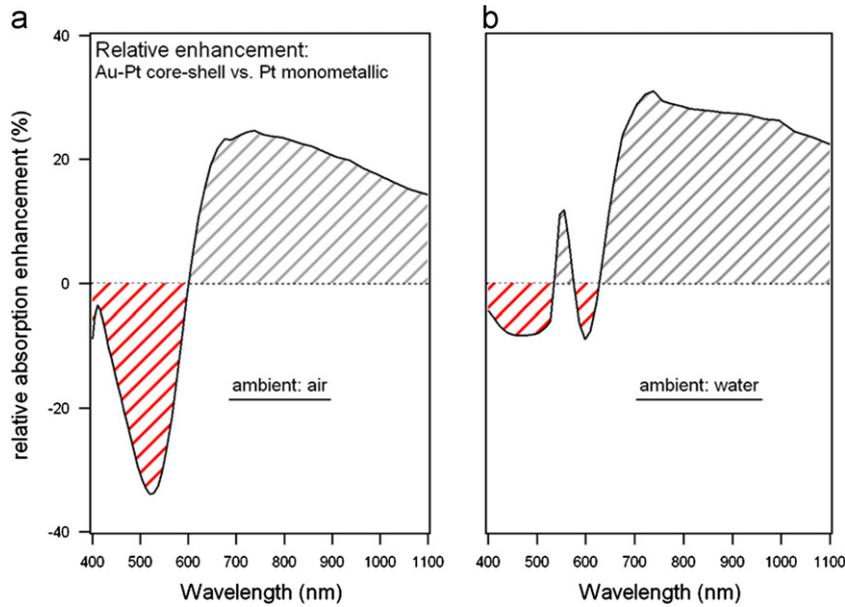
Fig. 7. Difference of the respective absorption enhancement curves of Fig. 6 of Au–Pt core–shell structures (Pt shell of 2 nm thickness) and monometallic Pt structures in air (a) and water (b).
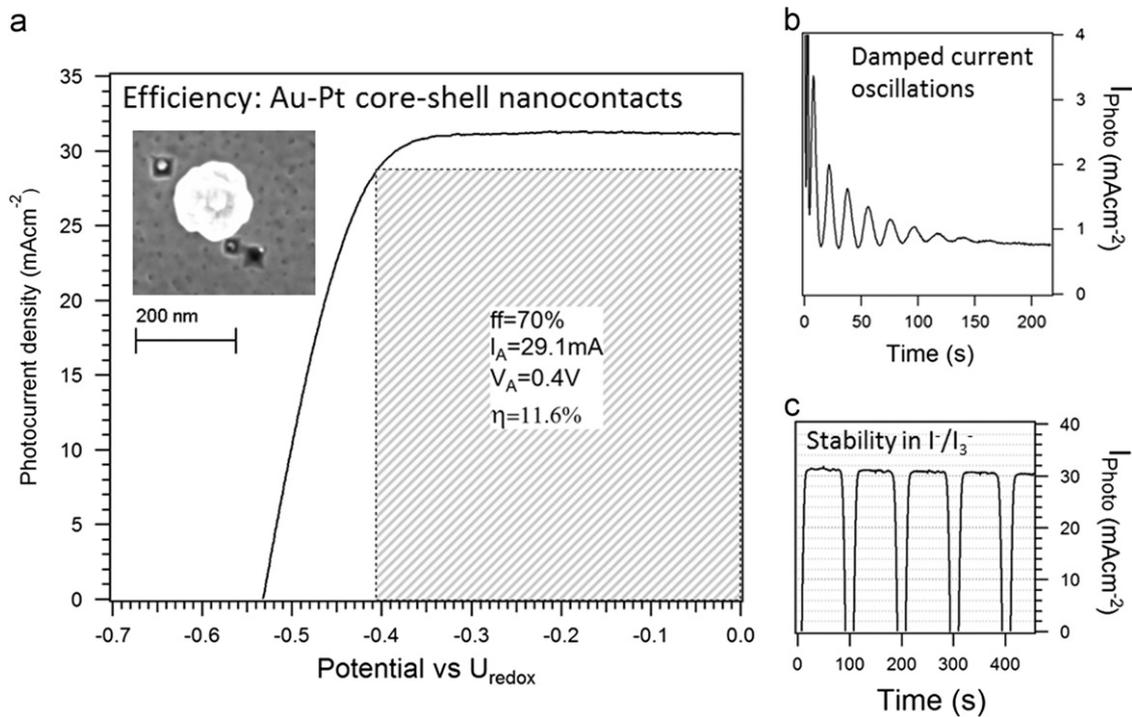

Fig. 8. Photocurrent behavior of the Au–Pt/SiO$_2$/Si interface in I$^-$/I$_3^-$. The potential is indicated with respect to the I$^-$/I$_3^-$ redox potential. (a) Current–voltage curve. The inset indicates the surface topography after SiO$_2$ formation in more acidic solutions of NH$_4$F (pH2) and after metal deposition. (b) Anodic oxide formation by damped photocurrent oscillations at pH2. (c) Assessment of the stability of the interface in the iodide/triiodide redox electrolyte.

environment. For application in air, the marked loss of absorption in the range $400 < \lambda < 600$ nm has to be taken into account.

Experimental results, shown in Fig. 2a, suggest a surface coverage of only about 7%. A lower absorption enhancement of about 11% ($\lambda > 500$ nm) and 20% ($\lambda > 650$ nm) has to be expected for this interface. Finally, variation of the oxide thickness (0–10 nm) resulted in negligible variations in the calculated absorption enhancements.

3.3. Cell efficiency and stability

The results of the preceding sections show that the porous SiO$_2$/Si interface permits the formation of complex metal heterostructures on silicon which combine the rectifying behavior of Schottky-like nanocontacts with the pronounced optical activity of plasmonic particles. For comparative assessment of the photoelectrochemical performance with and without plasmonic effects, however, nearly

stable operation in the I^-/I_3^- redox electrolyte is required. Cell degradation can proceed at the SiO_2/Si interface as well as at the interfacial region of the semiconductor-oxide-metal nanojunctions. For instance, pores not filled by metals or insufficiently covered by an oxide (see Fig. 2a and b) are susceptible to instant corrosive reactions upon exposure to the electrolyte. Surface and interface states may then be formed, reducing the potential across the depletion region in the semiconductor while surface recombination currents will limit the maximum photocurrent densities [23,24].

As indicated above, the preparation of anodic oxides at pH4 results in a high density of very small pores. These nanopores, if not filled by the metals, are assumed to provide capillary channels to the silicon interface and to induce accelerated cell degradation. More acidic solutions (pH2), in turn, lead to strongly damped photocurrent oscillations (see Fig. 8b) while the density of nanopores is considerably reduced (see inset in Fig. 8a). Consecutive photocurrent cycles, obtained in the I^-/I_3^- redox electrolyte, are shown in Fig. 8c and confirm only a slow decrease of the maximum photocurrent density from 31.5 mA cm^{-2} to 30 mA cm^{-2} after about 450 s. Moreover, the photovoltage of 0.53 V vs. the redox potential appears preserved. The overall efficiency of the Au–Pt core–shell device amounts to 11.6% during the first photocurrent cycle and the fill factor is 70%. Compared to the interface with monometallic Pt-nanocontacts, an enhancement of the efficiency by 0.9% (0.4%)[1], of the fill factor by 7% (5%), and of the photovoltage by 50 mV (30 mV) is achieved [11,12]. Maximum photocurrent densities (short circuit current), in turn, remained lower than reported for the monometallic interface. This effect, however, is attributed to the different setup of the electrochemical cell in [11,12] which allowed ultra-thin coverage of the samples by the iodide/triiodide electrolyte. The gain in efficiency observed here is assumed to mainly result from an optically induced increase of photoinduced minority charge carriers in a surface-near region. Consequently, the difference of the respective Fermi-levels of electrons and (photoinduced) holes at the surface, $\Delta A = |E_F^n - E_F^p|$, increases too. Here, A denotes the Helmholtz free energy as a measure of usable work that can be realized by the system. It appears therefore likely that the observed increase of the photovoltage by 50 mV (30 mV), $U_{ph} = (1/e)\Delta A$, is related to the optical activity of the Au–Pt core–shell structures. Together with the improved device stability, this increase improves then both fill factor and cell efficiency. It should be also noted that the relatively large particle diameter (100–200 nm), prepared here, has two distinguishable effects. Firstly, forward scattering is much more effective for an increased particle size as discussed in Section 3.2. Secondly, the width of the (semi-spherical) depletion region beneath the particles increases as well [25–27]. The observation that the efficiency enhancement of 0.9% (0.4%) is smaller than deduced from theoretical calculations is finally attributed to (i) an average particle size smaller than theoretically assumed and ii) a thicker electrolyte film in our electrochemical cell setup. In summary, optical as well as electronic interface properties appear clearly improved by the devised cell architecture, and the concept of electrochemical interface development can be regarded as promising fabrication route for both photoelectrochemical and solid-state solar cells.

4. Conclusion

Self-organized electrochemical fabrication principles were applied to realize a photoelectrochemical solar cell design with plasmonic Au–Pt core–shell nanostructures. Surface sensitive chemical and topographical investigations proved the successful

formation of Au–Pt nanocomposits at a porous SiO_2/Si interface. Considerable enhancement of light absorption, compared to monometallic Pt-nanocontacts, was deduced from Mie scattering analysis and FDTD simulations. Test operation in I^-/I_3^- redox electrolytes confirmed the improvement particularly of the photovoltage, of the fill factor and therefore of the cell efficiency. Limitations of the device stability could be circumvented by modified electrochemical preparation of the passivating SiO_2 layer. The findings demonstrate that electrochemical methods can be successfully applied to achieve specific optical and electronic properties in photovoltaic device architectures.

References

[1] K.R. Catchpole, A. Polman, Plasmonic solar cells, Optics Express 16 (2008) 21793–21800.
[2] H.A. Atwater, A. Polman, Plasmonics for improved photovoltaic devices, Nature Materials 9 (2010) 205–213.
[3] D.M. Schaadt, B. Feng, E.T. Yu, Enhanced semiconductor optical absorption via surface plasmon excitation in metal nanoparticles, Applied Physics Letters 86 (2005) 063106.
[4] D. Derkacs, S.H. Lim, P. Matheu, W. Mar, E.T. Yu, Improved performance of amorphous silicon solar cells via scattering from surface plasmon polaritons in nearby metallic nanoparticles, Applied Physics Letters 89 (2006) 093103.
[5] S. Pillai, K.R. Catchpole, T. Trupke, M.A. Green, Surface plasmon enhanced silicon solar cells, Journal of Applied Physics 101 (2007) 093105.
[6] I. Thomann, B.A. Pinaud, Z. Chen, B.M. Clemens, T.F. Jaramillo, M.L. Brongersma, Plasmon enhanced solar-to-fuel energy conversion, Nano Letters 11 (2011) 3440–3446.
[7] C. Hägglund, M. Zäch, B. Kasemo, Enhanced charge carrier generation in dye sensitized solar cells by nanoparticle plasmons, Applied Physics Letters 92 (2008) 013113.
[8] T. Kawasaki, Y. Takahashi, T. Tatsuma, Enhancement of dye-sensitized photocurrents by gold nanoparticles: effects of dye–particle spacing, Nanoscale 3 (2011) 2865–2867.
[9] P.H. Qi, J.B. Hiskey, Dissolution kinetics of gold in iodide solutions, Hydrometallurgy 27 (1991) 47–62.
[10] M. Aggour, K. Skorupska, T. Stempel Pereira, H. Jungblut, J. Grzanna, H.J. Lewerenz, Photoactive silicon-based nanostructure by self-organized electrochemical processing, Journal of Electrochemical Society 154 (2007) H794–H797.
[11] H.J. Lewerenz, T. Stempel, Efficient Solar Cell Structure Prepared by Electrodeposition into oscillation-induced nanoporous silicon oxide, ECS Transactions 16 (2008) 375–389.
[12] Th. Stempel-Pereira, Effiziente selbstorganisierteSilicium-Nanoemitter-Solarzellen: Oberflachenanalyse undPhotoelektrochemie, Doctoral Thesis, Technical University Berlin, 2011.
[13] M. Lublow, H.J. Lewerenz, Fractal photocorrosion of silicon electrodes in concentrated ammonium fluoride, Electrochemical and Solid State Letters 10 (2007) C51–C55.
[14] M. Lublow, H.J. Lewerenz, Brewster-angle analysis of native and photoelectrochemically grown silicon oxide nanotopographies, Surface Science 601 (2007) 4227–4231.
[15] J. Grzanna, T. Notz, T. Stempel, H.J. Lewerenz, Structure formation at the nanometric scale during current oscillations at the Si/electrolyte contact, Physica Status Solidi C 8 (2010) 1734–1738.
[16] M. Lublow, H.J. Lewerenz, Real-time monitoring of $SiO_2/Si(111)$ interlayer etching by Brewster-angle reflectometry, Surface Science 602 (2008) 1677–1687.
[17] M. Lublow, K. Skorupska, S. Zoladek, P.J. Kulesza, T. Vo-Dinh, H.J. Lewerenz, On the behaviour of Au plasmonic nanoparticles during hydrogen evolution at p-Si, Electrochemical Communications 12 (2010) 1298–1301.
[18] J.J. Yeh, I. Lindau, Atomic subshell photoionization cross sections and asymmetry Parameters: $1 < Z < 103$, Atomic Data and Nuclear Data Tables 32 (1985) 1–155.
[19] U. Kreibig, M. Vollmer, Optical Properties of Metal Clusters, Springer-Verlag, Berlin Heidelberg, 1995.
[20] C.F. Bohren, D.R. Huffman, Scattering of Light by Small Particles, John Wiley and Sons Inc., 1983.
[21] G. Mie, Beiträge zur Optik trüber Medien, speziell kolloidaler Metallösungen, Leipzig, Annalen der Physik 330 (1908) 377–445.
[22] C. Langhammer, Z. Yuan, I. Zoric, B. Kasemo, Plasmonic properties of supported Pt and Pd nanostructures, Nano Letters 6 (2006) 833–838.
[23] F. El Guibaly, K. Colbow, Theory of photocurrent in semiconductor-electrolyte junction solar cells, Journal of Applied Physics 53 (1982) 1737.
[24] F. El Guibaly, Surface barrier junctions: majority- and minority-carrier currents, Journal of Applied Physics 65 (1989) 1168.
[25] G.D.J. Smit, S. Rogge, T.M. Klapwijk, Scaling of nano-Schottky-diodes, Applied Physics Letters 81 (2002) 3852.
[26] N.V. Vostokov, V.I. Shashkin, Electrical properties of metal-semiconductor nanocontacts, Semiconductors 38 (2004) 1047–1052.
[27] C. Donolato, Approximate analytical solution to the space charge problem in nanosized Schottky diodes, Journal of Applied Physics 95 (2004) 2184.

---

[1] Numbers in brackets refer to a Doctoral Thesis, not available in English (see Ref. [12]).